Supporting Information

Regulating the Phase Stability and Bandgap of Quasi-2D Dion–Jacobson $CsSnI_3$ Perovskite *via* Intercalating Organic Cations

Qian Sun,[1,2] Zhi Fang,[1,2] Yapeng Zheng,[1,2] Zuobao Yang,[2] Feng Hu,[2] Yang Yang,[2] Weiyou Yang,[2] Xinmei Hou,[1,] and Ming-Hui Shang[2,3,*]*

[1] Beijing Advanced Innovation Center for Materials Genome Engineering, Collaborative Innovation Center of Steel Technology, University of Science and Technology Beijing, Beijing 100083, China.

[2] Institute of Micro/Nano Materials and Devices, Ningbo University of Technology, Ningbo City 315016, P. R. China.

[3] Graduate School of Advanced Integration Science, Chiba University, 1-33 Yayoi-cho, Inage, Chiba 263-8522, Japan.

*To whom correspondence should be addressed: Email: houxinmeiustb@ustb.edu.cn (X. Hou), shangminghui@nbut.edu.cn (M.-H. Shang).

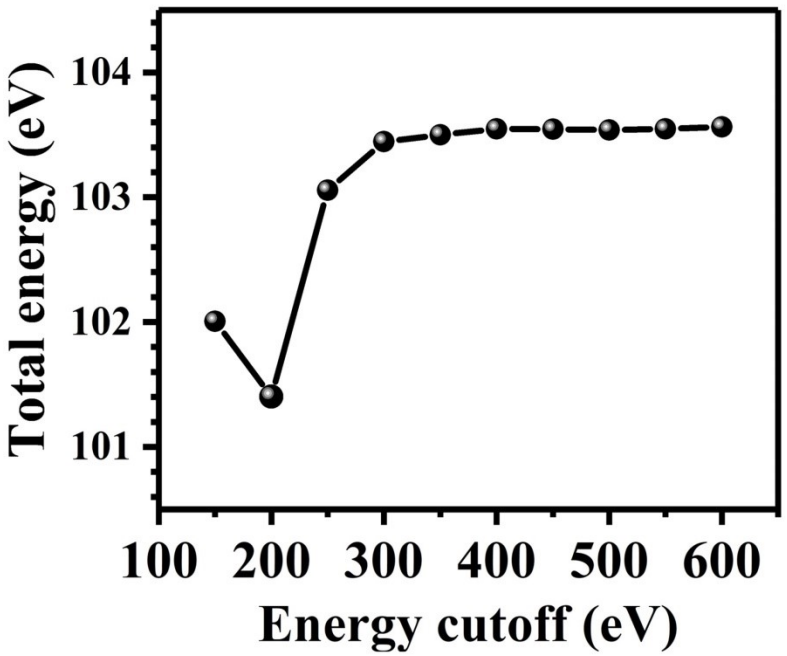

Figure S1. The convergence test of different cutoff energy of quasi-2D DJ (ThDMA)$Cs_{n-1}Sn_nI_{3n+1}$ perovskites.

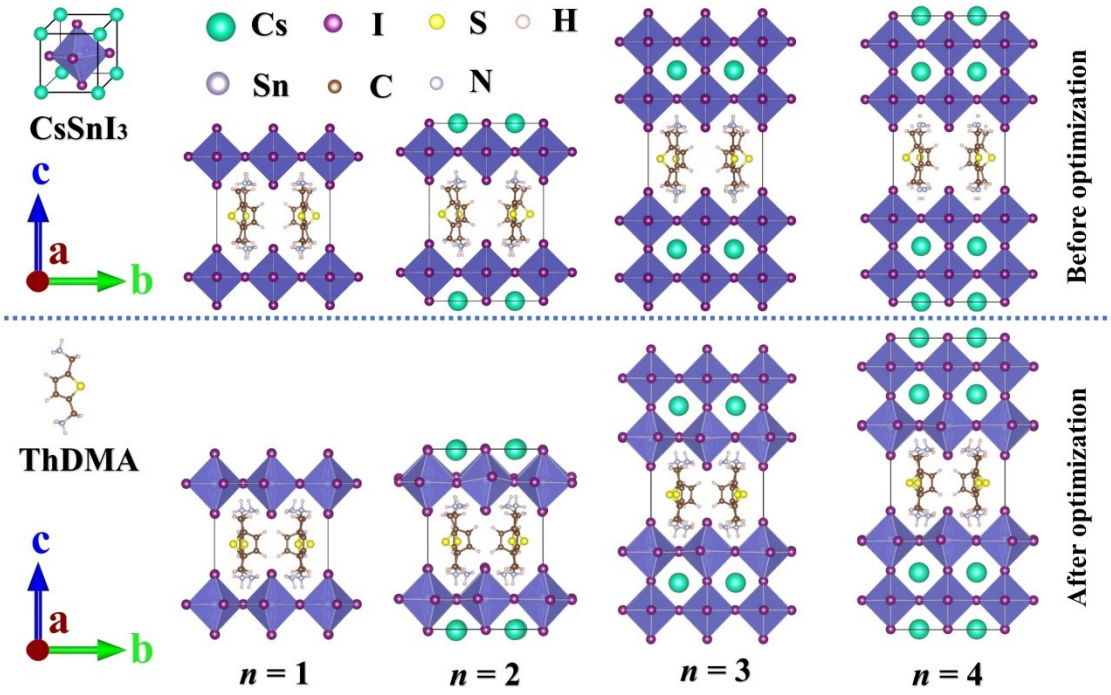

Figure S2. Configurations before/after geometry optimization of quasi-2D DJ (ThDMA)$Cs_{n-1}Sn_nI_{3n+1}$ perovskites from n = 1 to 4. The structures of $CsSnI_3$ unit and cation $ThDMA^{2+}$ are given in illustration.

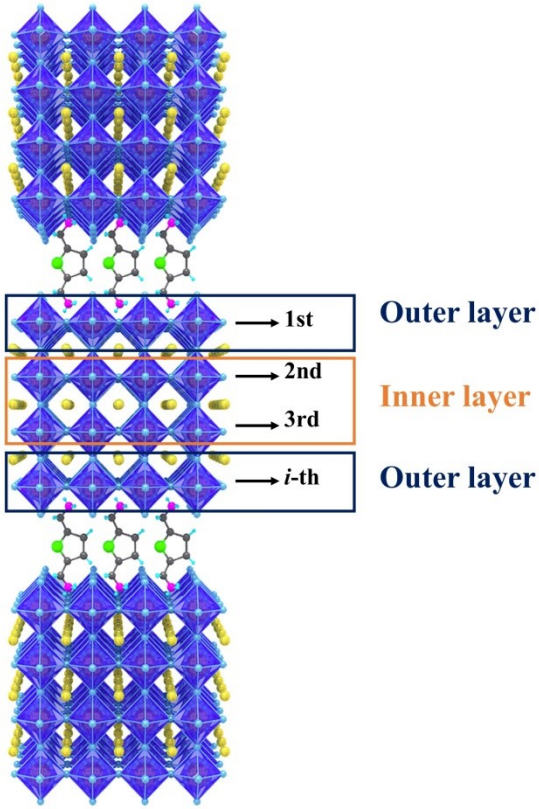

Figure S3. Illustration on serial numbers of *i*-th inorganic layer and the definition of outer and inner layer.

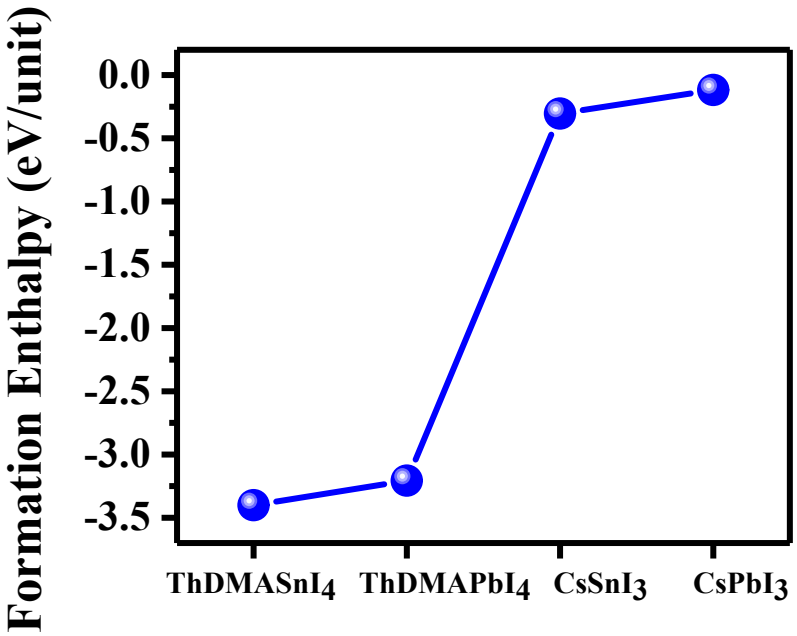

Figure S4. Formation enthalpies of $ThDMAPbI_4$, $ThDMASnI_4$, $CsPbI_3$ and $CsSnI_3$ perovskites.

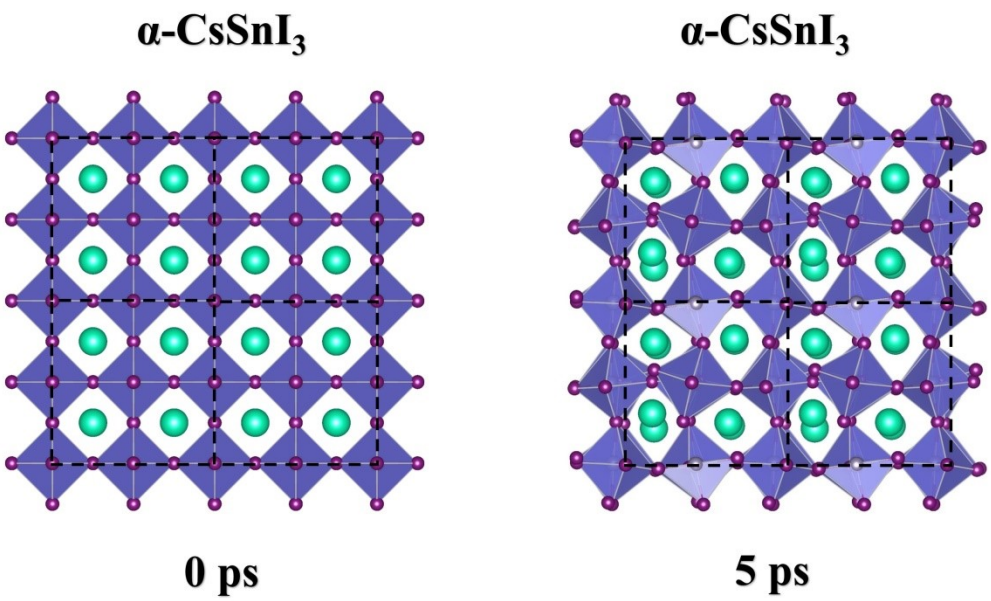

Figure S5. The structures of $CsSnI_3$ perovskites after AIMD simulation at 0 and 5 ps under 300 K, respectively.

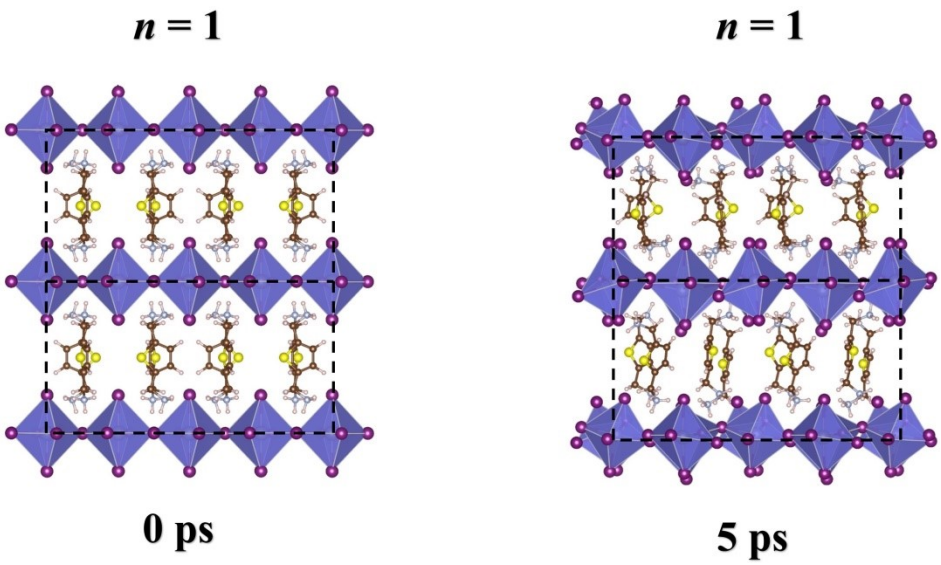

Figure S6. The structures of (ThDMA)$Cs_{n-1}Sn_nI_{3n+1}$ (n = 1) perovskites after AIMD simulation at 0 and 5 ps under 300 K, respectively.

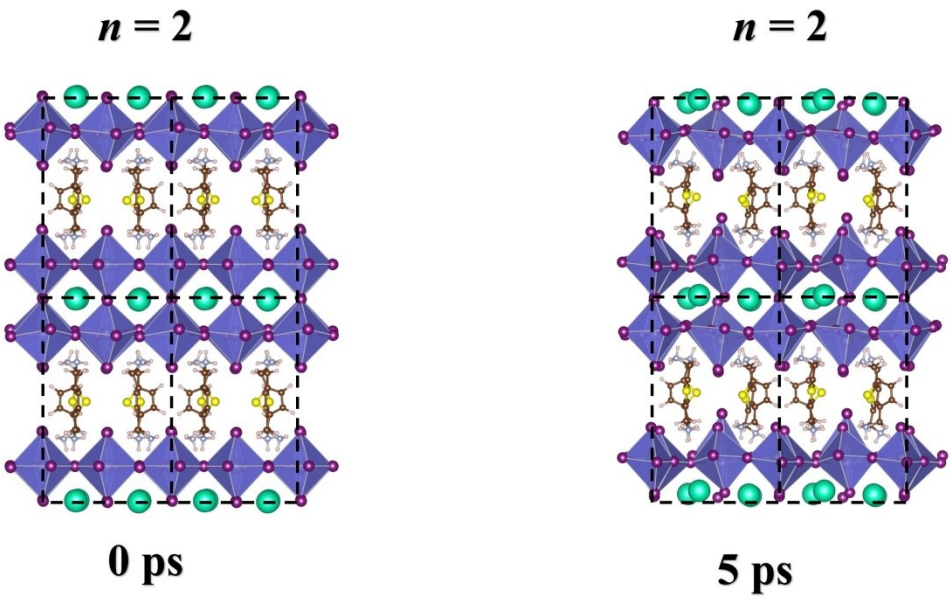

Figure S7. The structures of (ThDMA)$Cs_{n-1}Sn_nI_{3n+1}$ (n = 2) perovskites after AIMD simulation at 0 and 5 ps under 300 K, respectively.

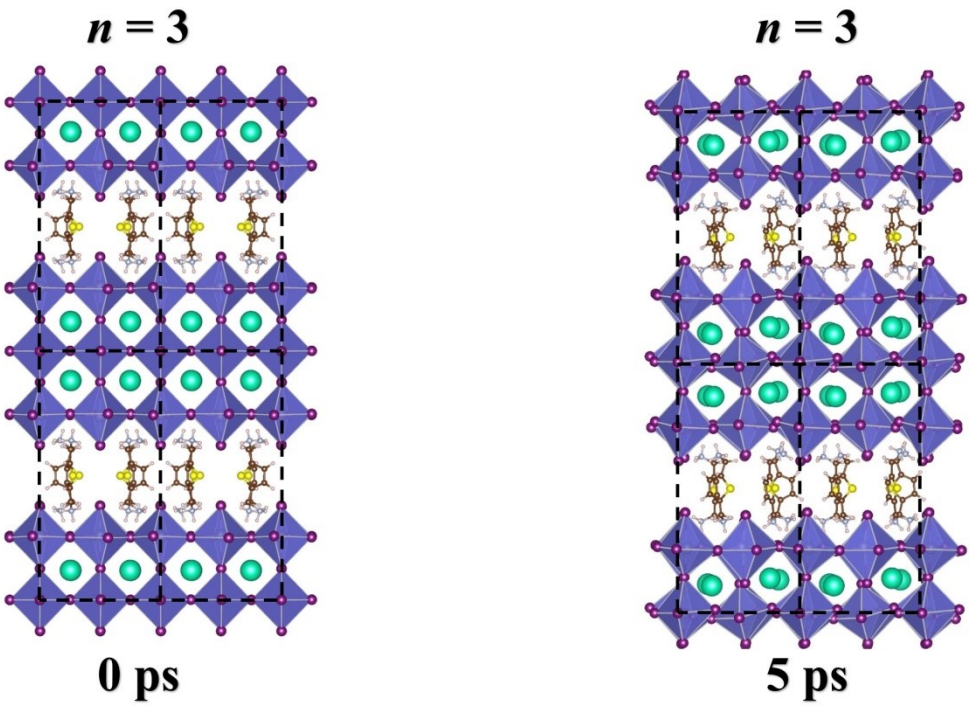

Figure S8. The structures of (ThDMA)$Cs_{n-1}Sn_nI_{3n+1}$ (n = 3) perovskites after AIMD simulation at 0 and 5 ps under 300 K, respectively.

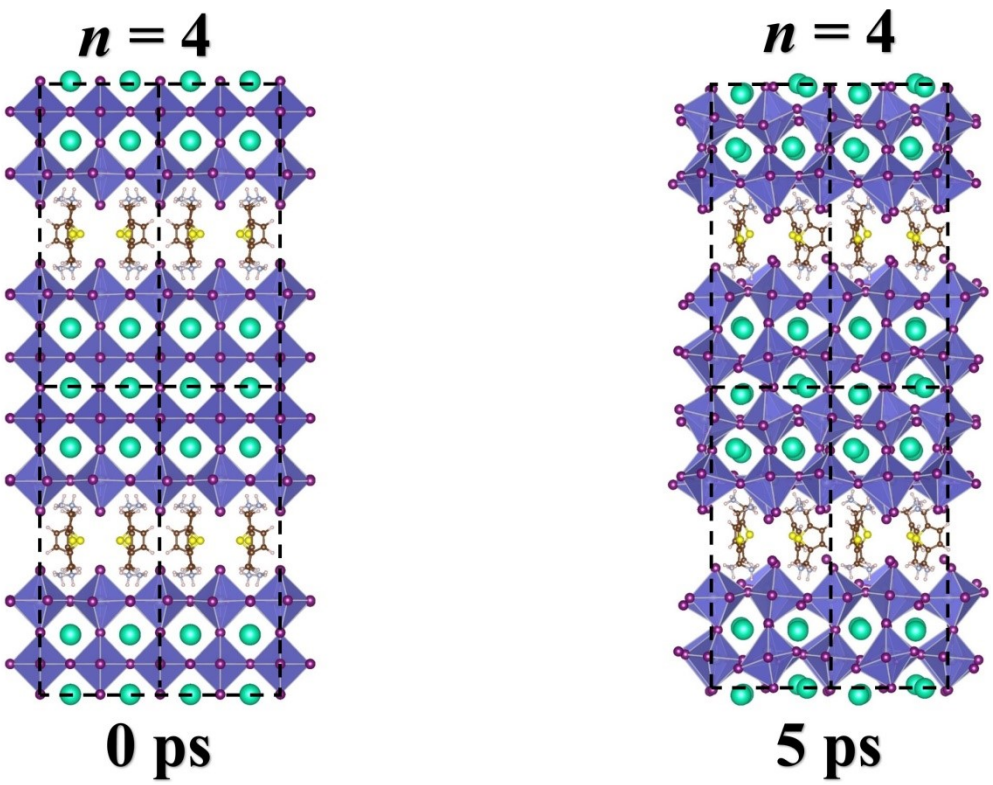

Figure S9. The structures of (ThDMA)$Cs_{n-1}Sn_nI_{3n+1}$ (n = 4) perovskites after AIMD simulation at 0 and 5 ps under 300 K, respectively.

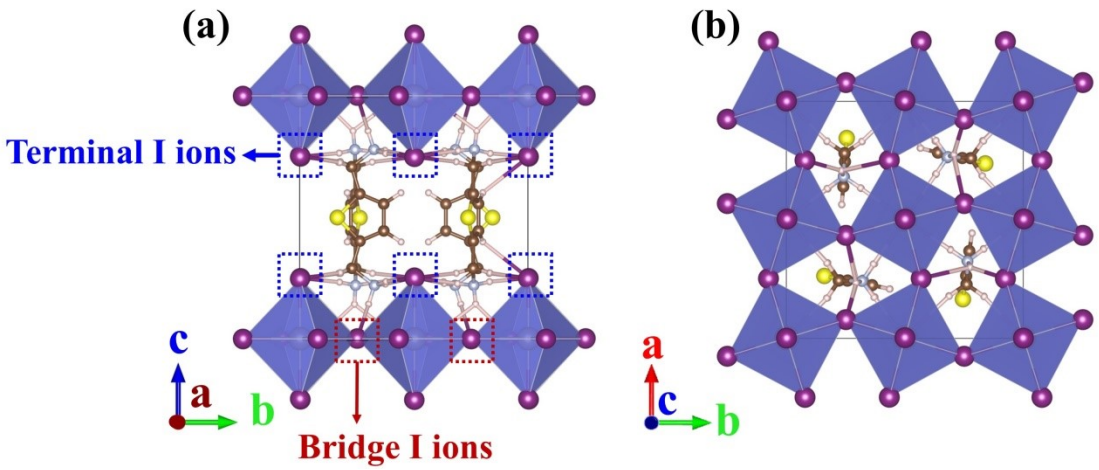

Figure S10. Illustration on I-H bonds of (ThDMA)$Cs_{n-1}Sn_nI_{3n+1}$ (n = 1).

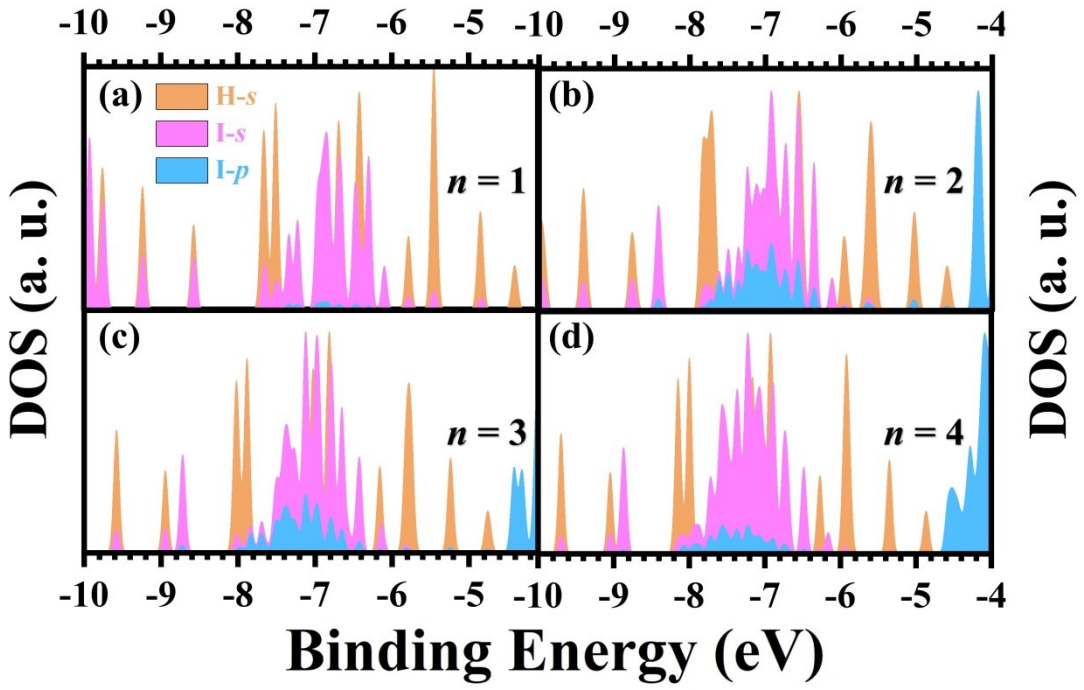

Figure S11. (a-d) Calculated PDOS of I and H atoms from I-H bonds of (ThDMA)$Cs_{n-1}Sn_nI_{3n+1}$ (n = 1-4), respectively.

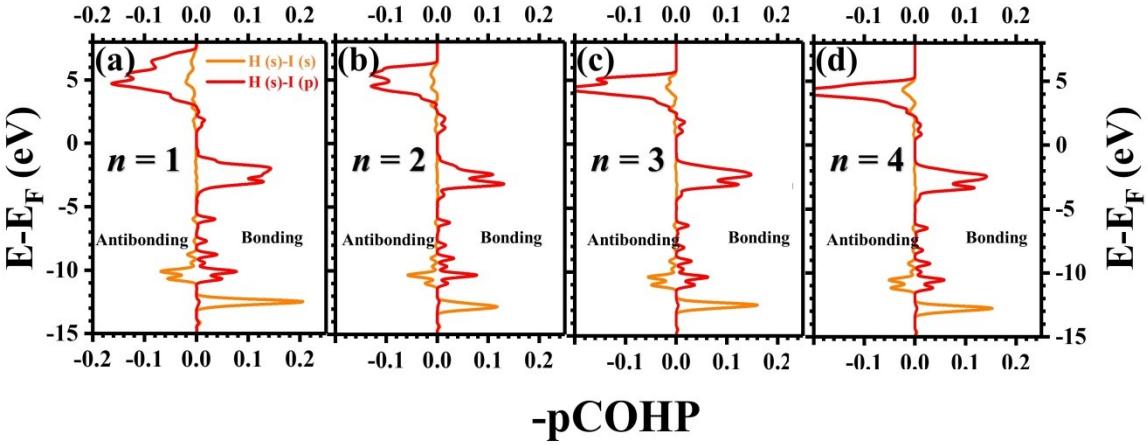

Figure S12. (a-d) Orbital-resolved COHP analysis for H and I atom of (ThDMA)$Cs_{n-1}Sn_nI_{3n+1}$ (n = 1-4), respectively.

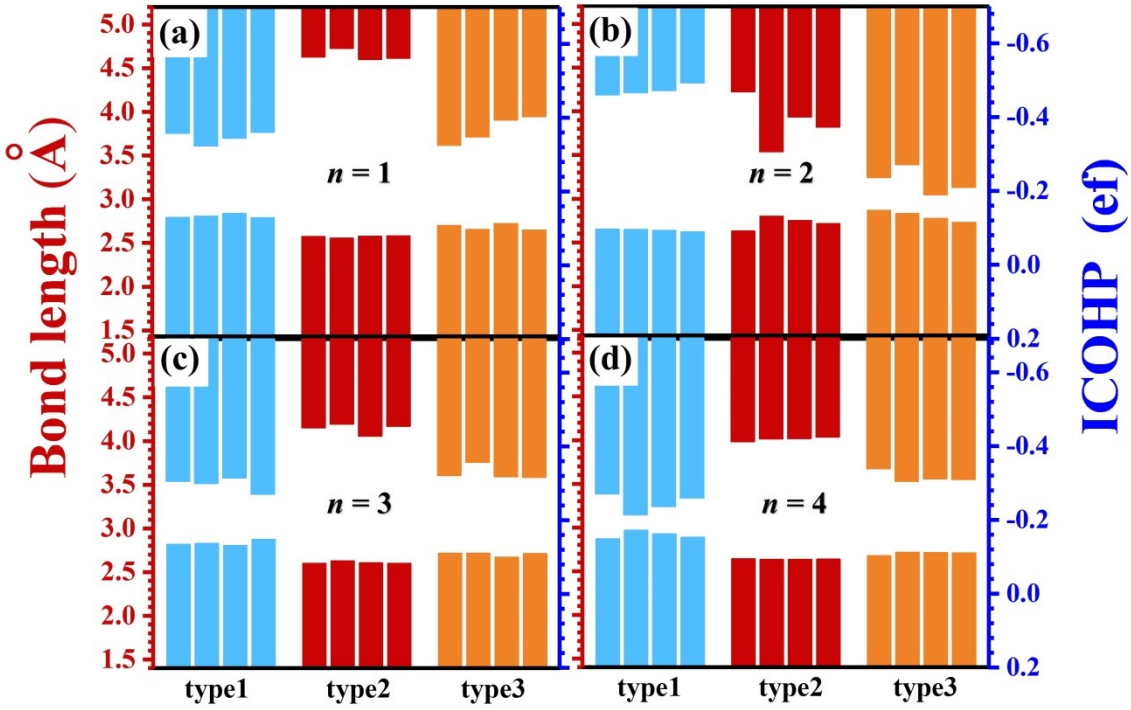

Figure S13. (a-d) The H-I bond length statistics and integrated crystal orbital Hamiltonian population (ICOHP) of (ThDMA)$Cs_{n-1}Sn_nI_{3n+1}$ (n = 1-4), respectively.

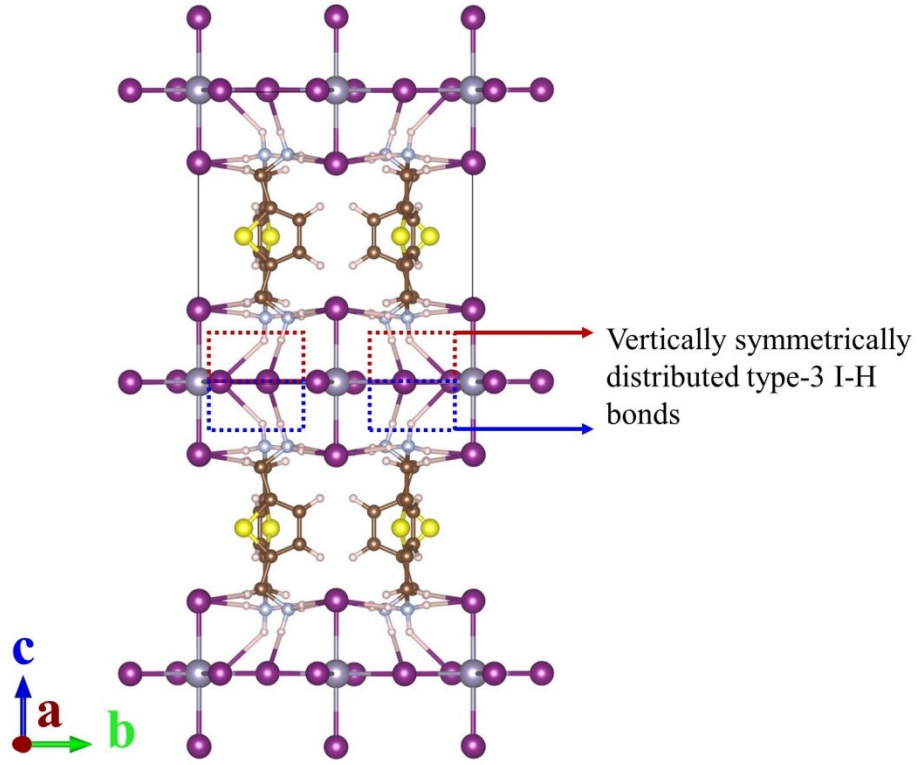

Figure S14. The type-3 I-H bonds vertically symmetrically distributed on both sides of the inorganic layer in (ThDMA)$Cs_{n-1}Sn_nI_{3n+1}$ (n = 1) from the side view.

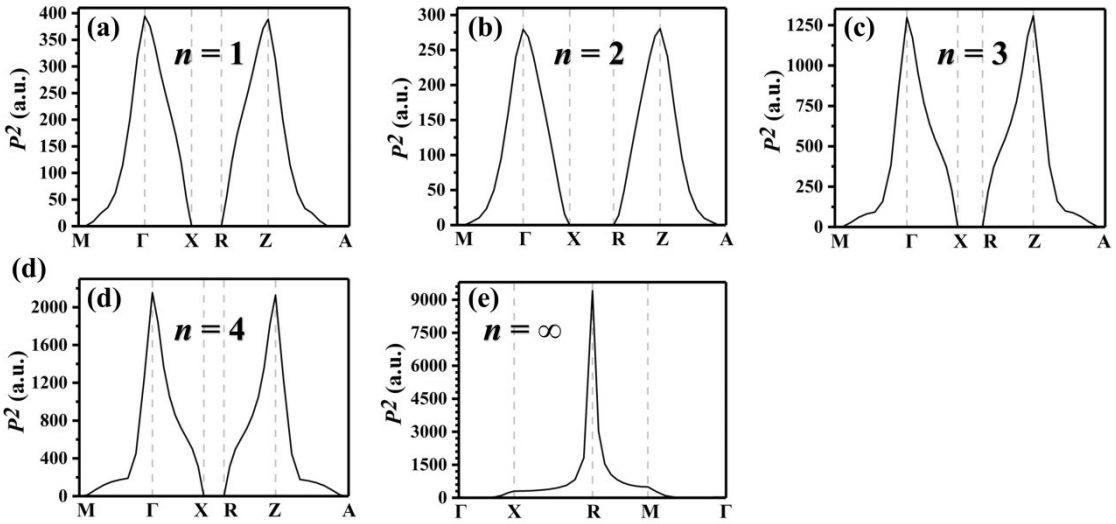

Figure S15. (a-e) The transition dipole moment (TDM) of (ThDMA)$Cs_{n-1}Sn_nI_{3n+1}$ (n = 1-4 and ∞) perovskites, respectively.

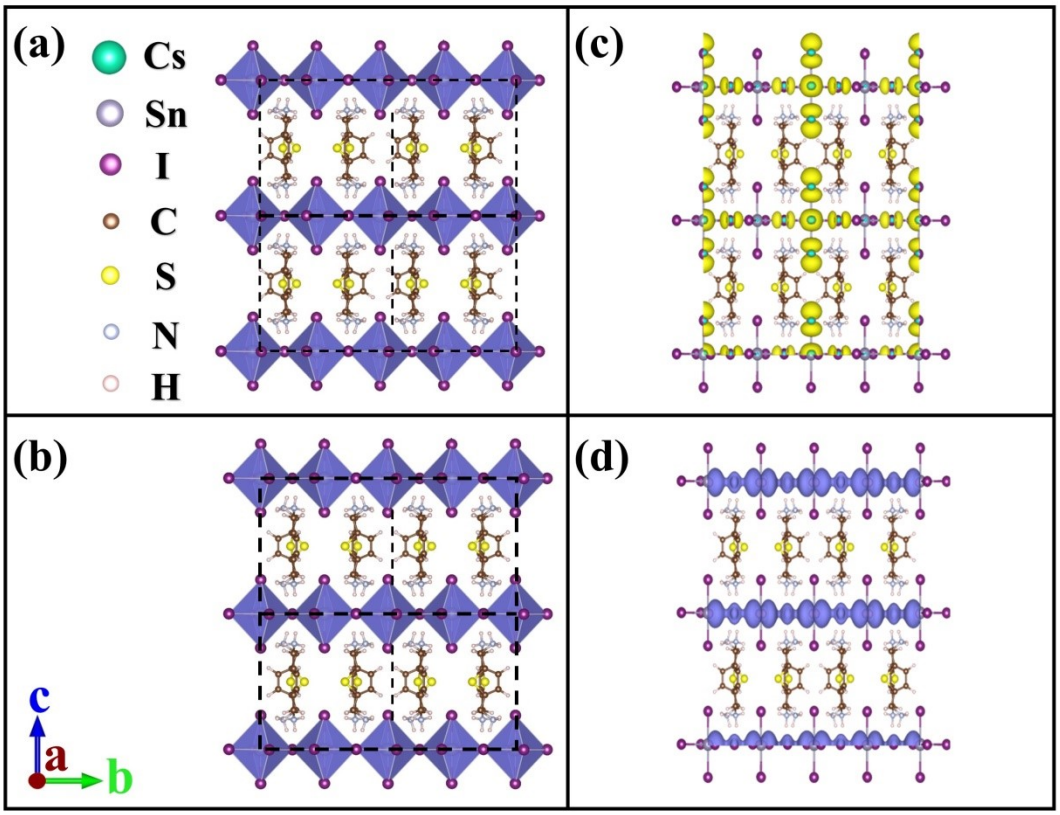

Figure S16. (a, b) The optimized polyhedron model of 1×2×2 supercell of (ThDMA)$Cs_{n-1}Sn_nI_{3n+1}$ (n = 1) from the side view and (c, d) its partial charge densities on VBM and CBM states in the (100) crystal plane, respectively.

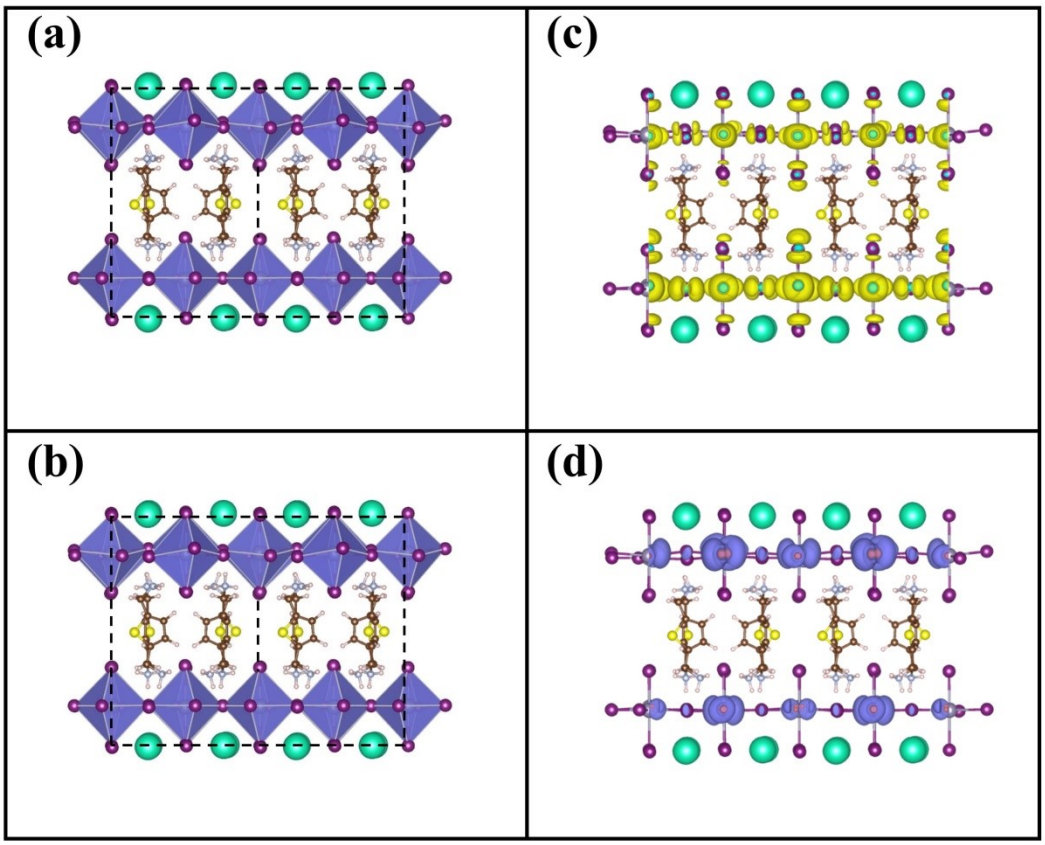

Figure S17. (a, b) The optimized polyhedron model of 1×2×2 supercell of (ThDMA)$Cs_{n-1}Sn_nI_{3n+1}$ (n = 2) from the side view and (c, d) its partial charge densities on VBM and CBM states in the (100) crystal plane, respectively.

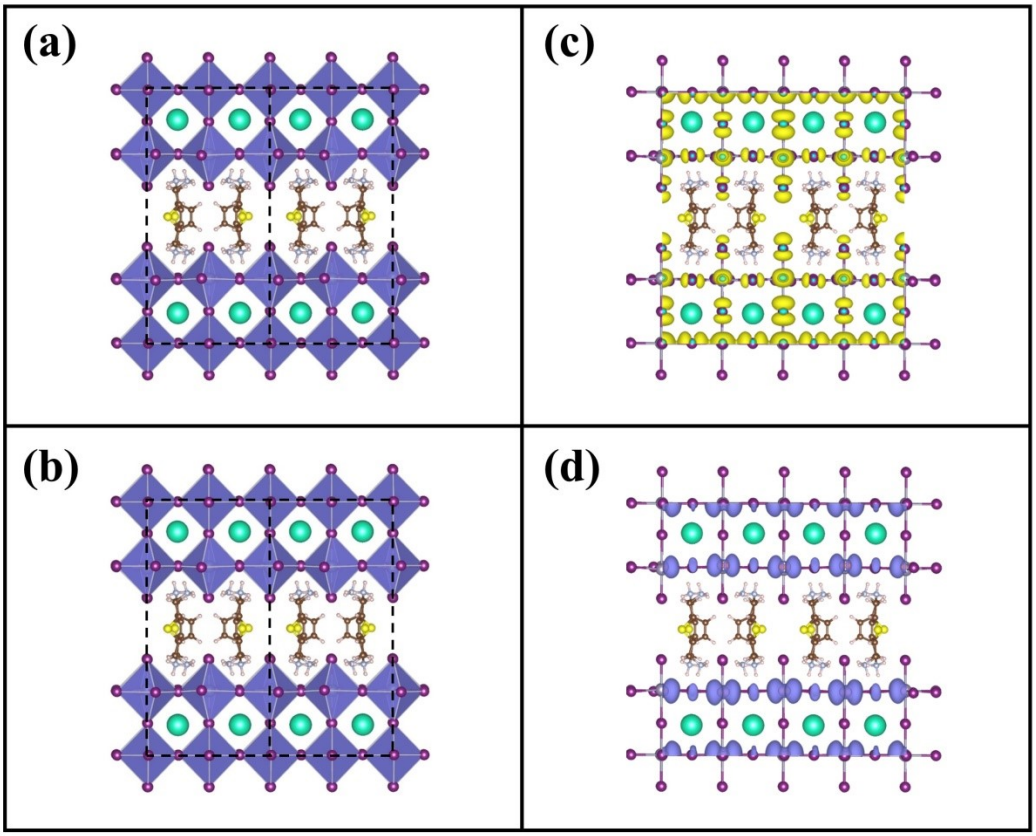

Figure S18. (a, b) The optimized polyhedron model of 1×2×2 supercell of (ThDMA)$Cs_{n-1}Sn_nI_{3n+1}$ (n = 3) from the side view and (c, d) its partial charge densities on VBM and CBM states in the (100) crystal plane, respectively.

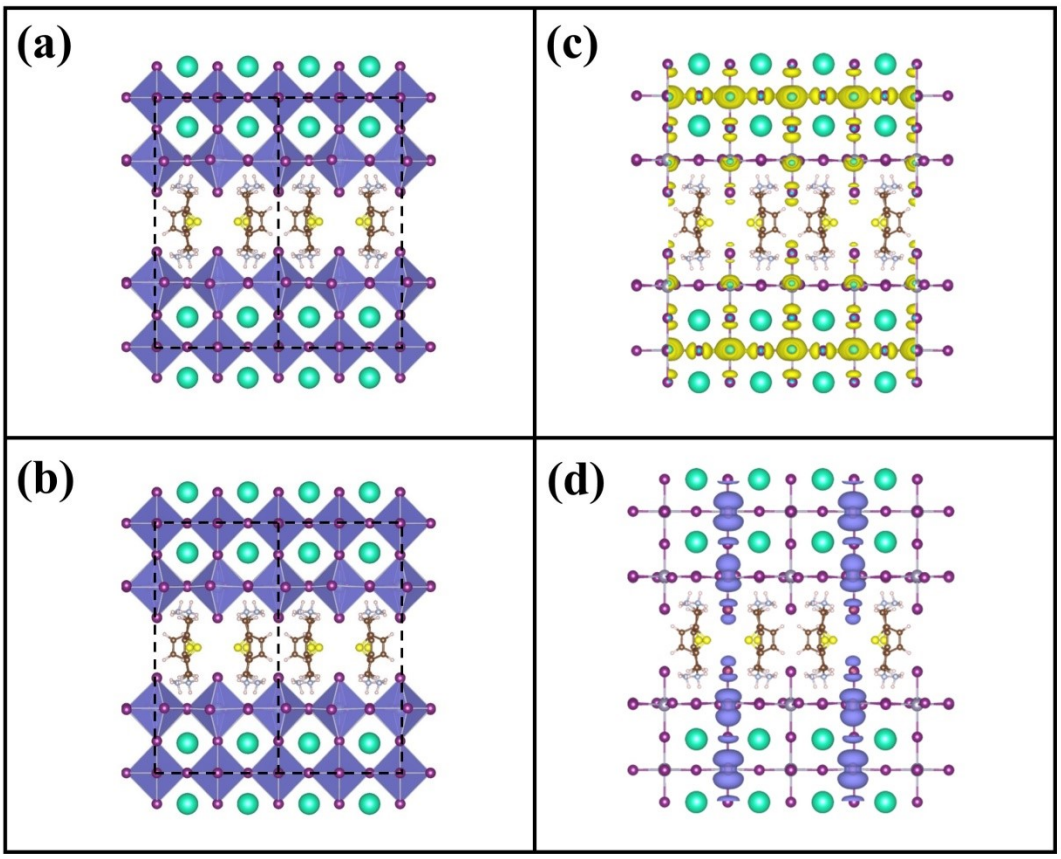

Figure S19. (a, b) The optimized polyhedron model of 1×2×2 supercell of (ThDMA)$Cs_{n-1}Sn_nI_{3n+1}$ (n = 4) from the side view and (c, d) its partial charge densities on VBM and CBM states in the (100) crystal plane, respectively.

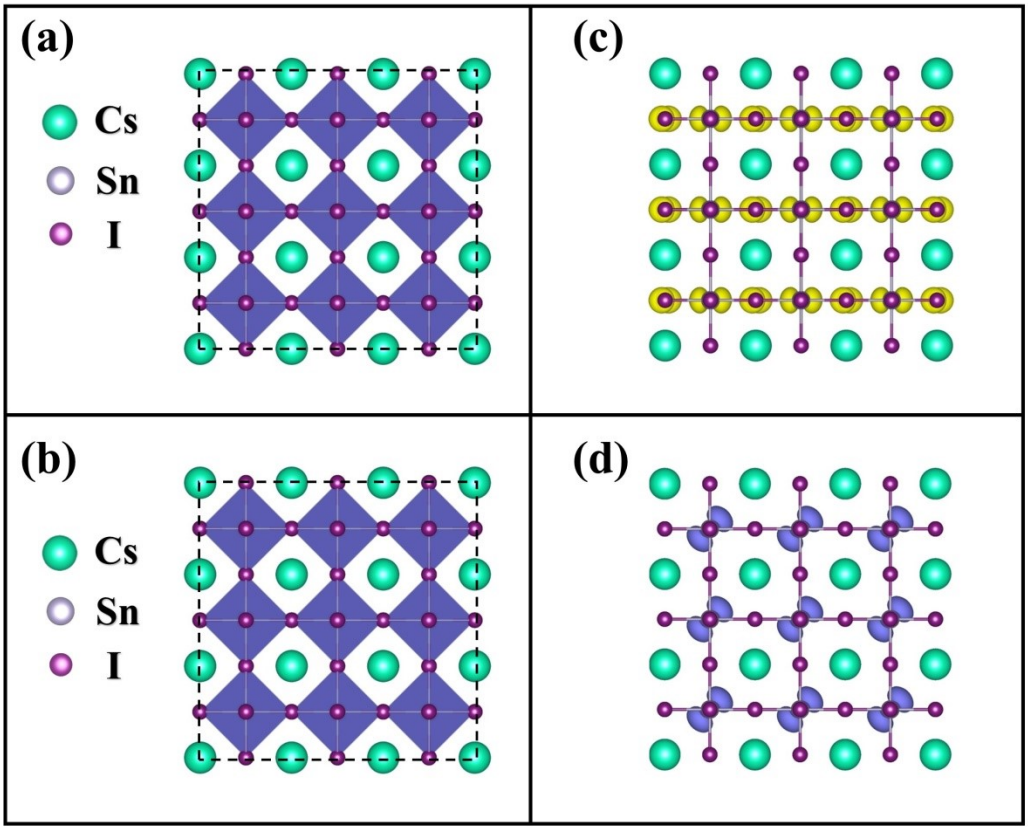

Figure S20. (a, b) The optimized polyhedron model of 3×3×3 supercell of $CsSnI_3$ unit cell and (c, d) its partial charge densities on VBM and CBM states, respectively.

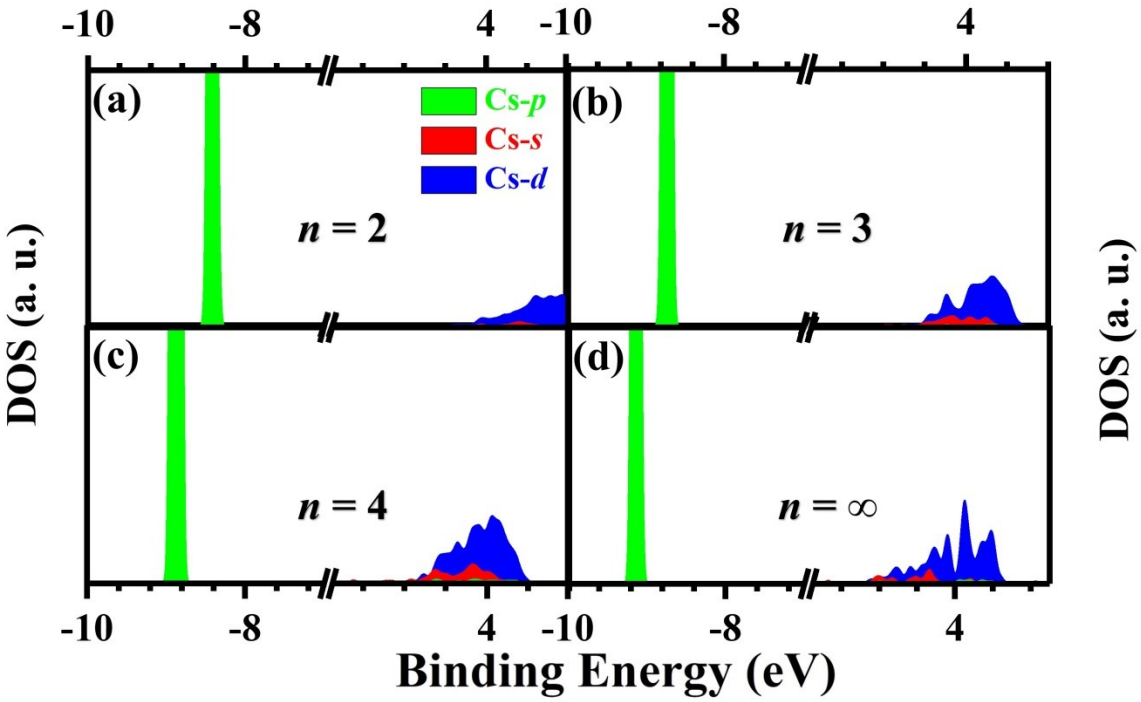

Figure S21. (a-d) Calculated PDOS of Cs^- ions in (ThDMA)$Cs_{n-1}Sn_nI_{3n+1}$ with n = 2, 3, 4 and ∞, respectively.

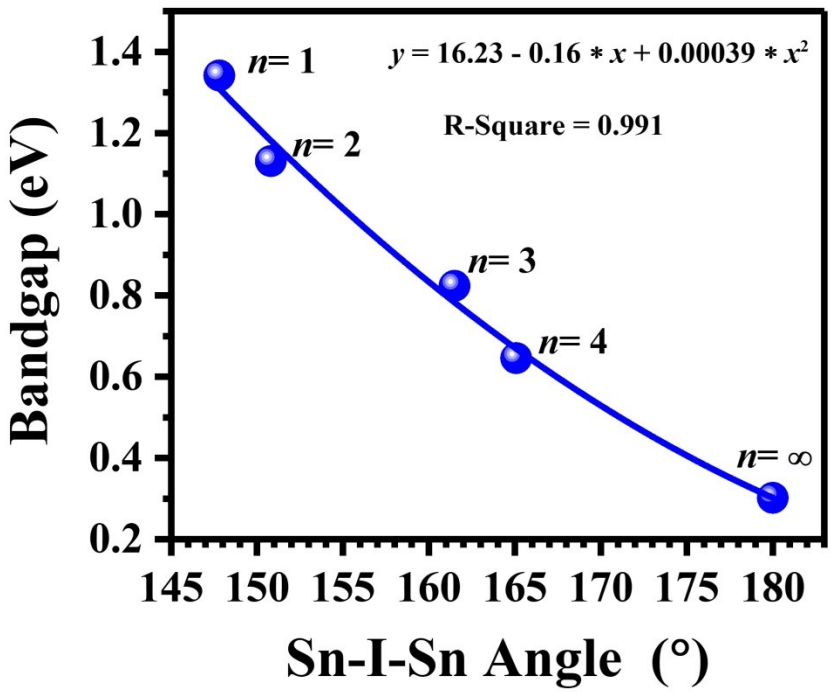

Figure S22. The calculated relationship between equatorial angles and bandgap employing polynomial fitting.

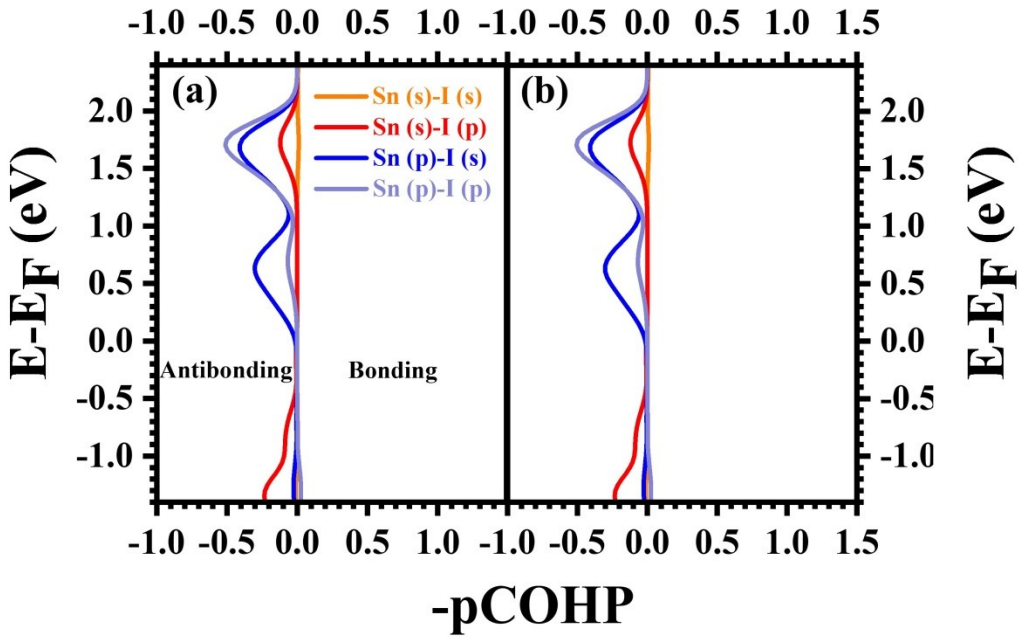

Figure S23. (a, b) Orbital-resolved COHP analysis for Sn and I atom of $CsSnI_3$ in (a) apical (vertical to inorganic layer) direction and (b) equatorial (parallel to inorganic layer) direction.

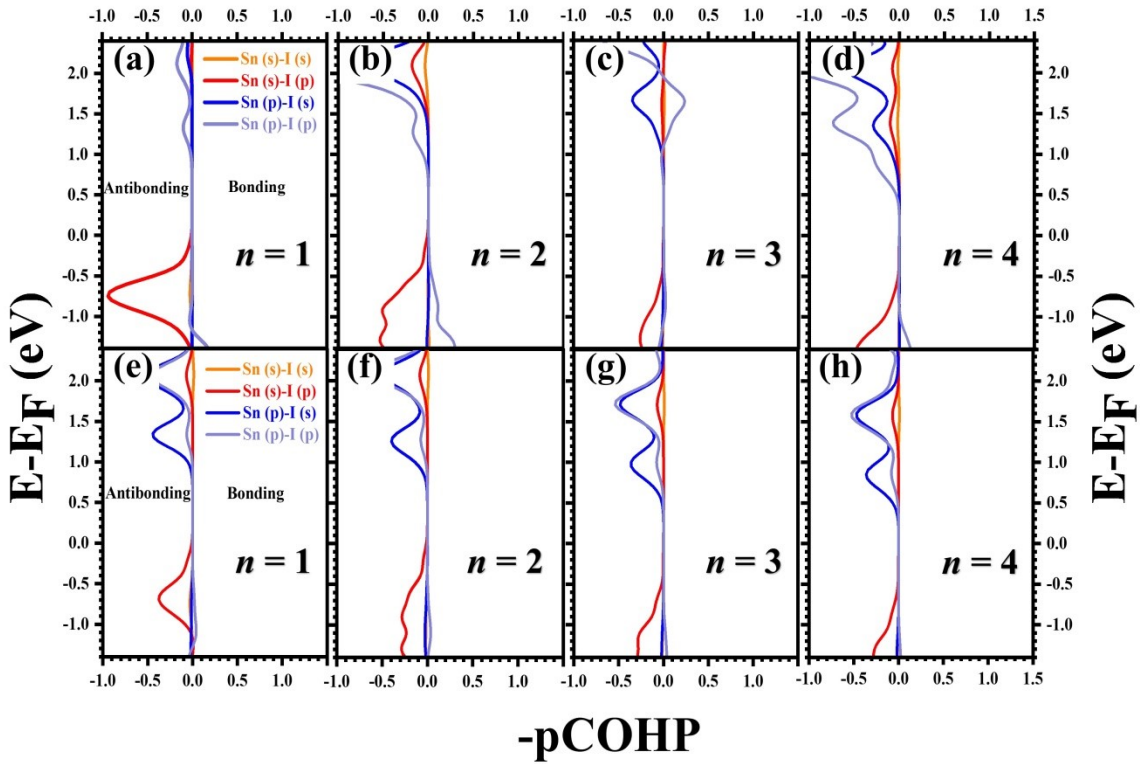

Figure S24. (a-h) Orbital-resolved COHP analysis for Sn and I atom of (ThDMA)$Cs_{n-1}Sn_nI_{3n+1}$ (*n* = 1-4) in (a-d) apical and (e-h) equatorial direction.

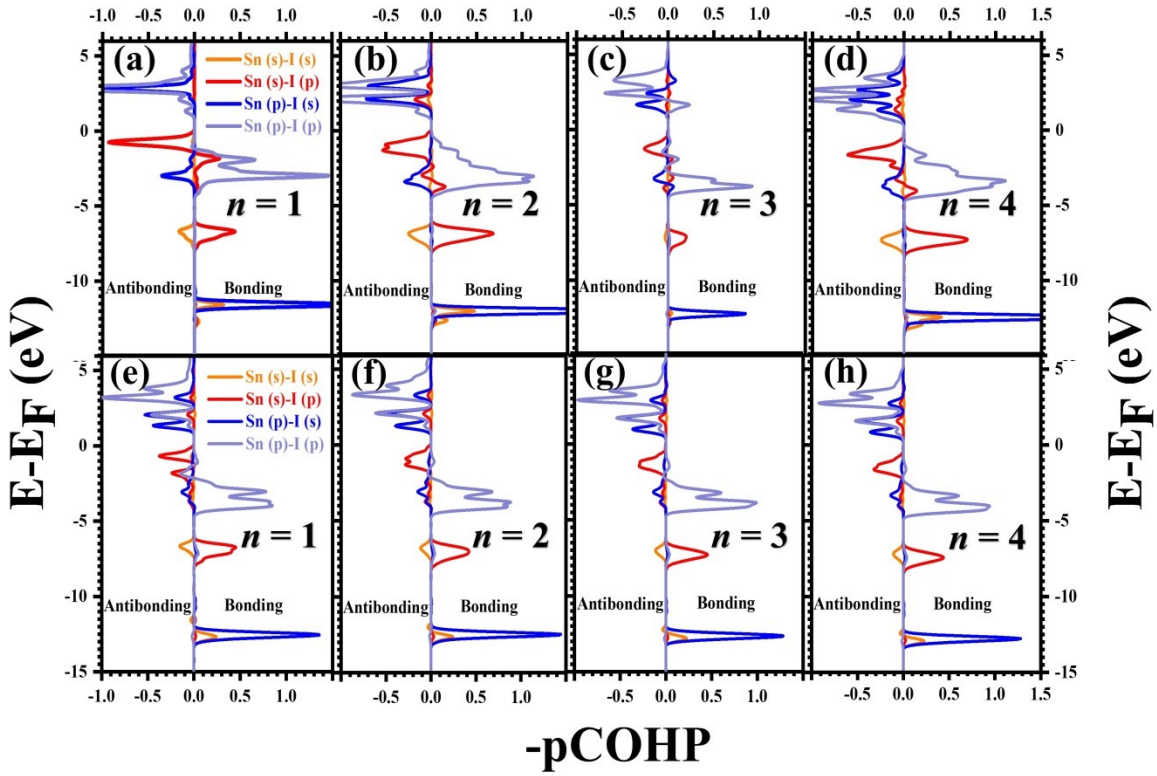

Figure S25. (a-h) Orbital-resolved COHP analysis for Sn and I atom of (ThDMA)$Cs_{n-1}Sn_nI_{3n+1}$ (n = 1-4) in (a-d) apical and (e-h) equatorial direction.

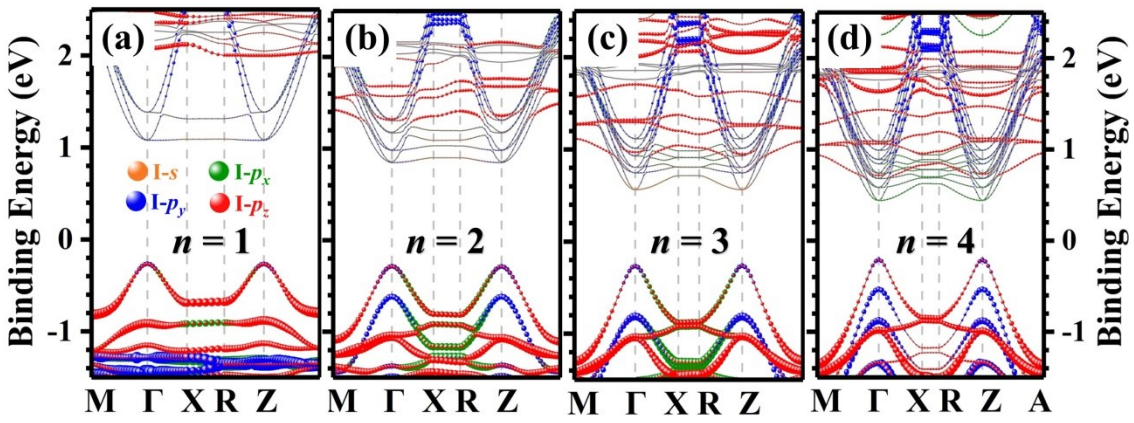

Figure S26. (a-d) Decomposed band structures of the *s*, *p* orbitals of I^- ions for (ThDMA)$Cs_{n-1}Sn_nI_{3n+1}$ (n = 1-4).

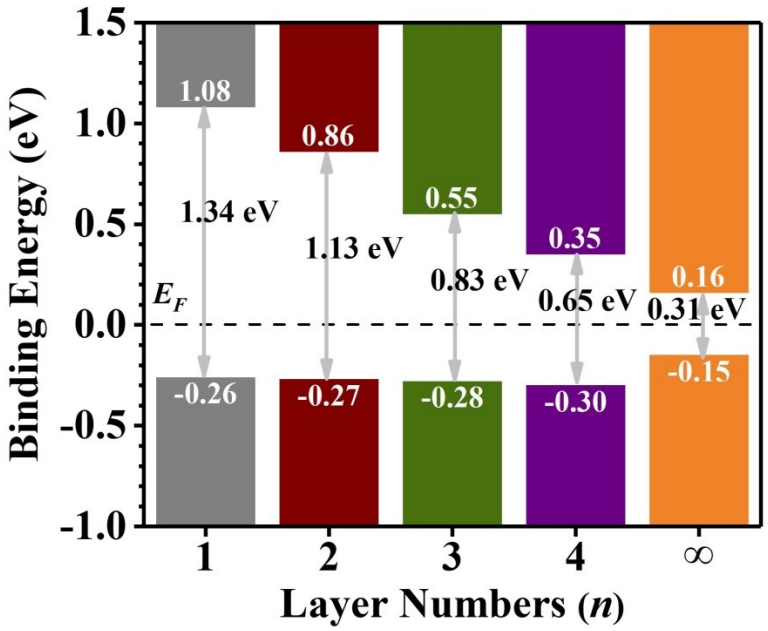

Figure S27. The calculated bandgap, energy level of CBM and VBM with respect to the Fermi level energies (Fermi level energies = 0).

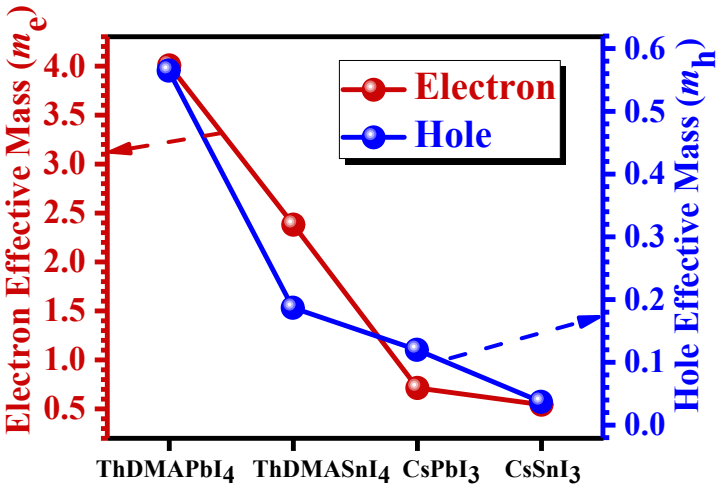

Figure S28. Hole and electron effective masses of $ThDMAPbI_4$, $ThDMASnI_4$, $CsPbI_3$ and $CsSnI_3$ perovskites.

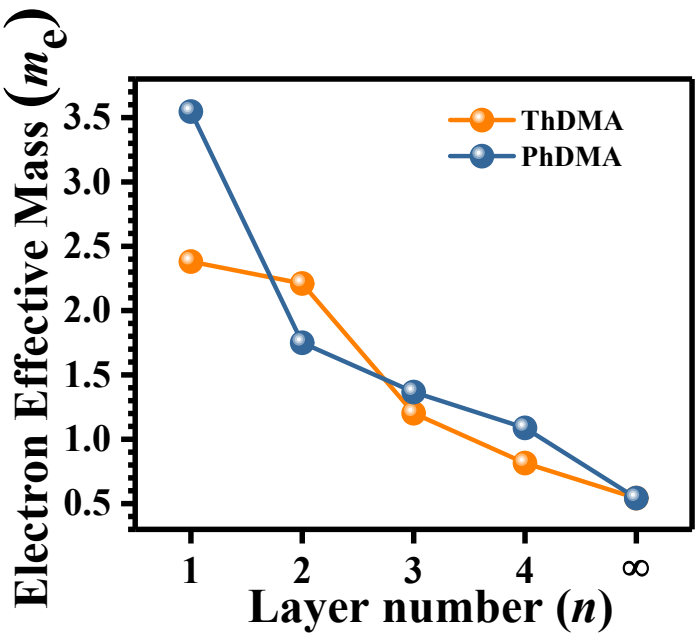

Figure S29. Electron effective masses of (ThDMA)$Cs_{n-1}Sn_nI_{3n+1}$ and (PhDMA)$Cs_{n-1}Sn_nI_{3n+1}$ perovskites.

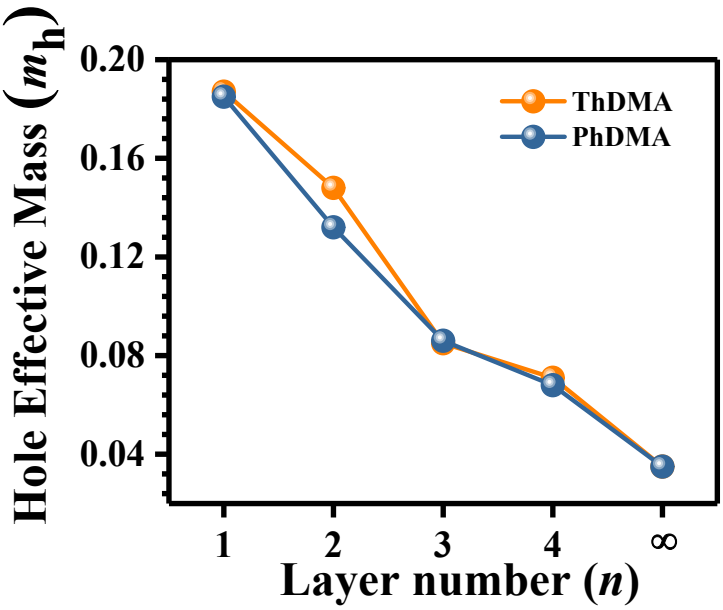

Figure S30. Hole effective masses of (ThDMA)$Cs_{n-1}Sn_nI_{3n+1}$ and (PhDMA)$Cs_{n-1}Sn_nI_{3n+1}$ perovskites.

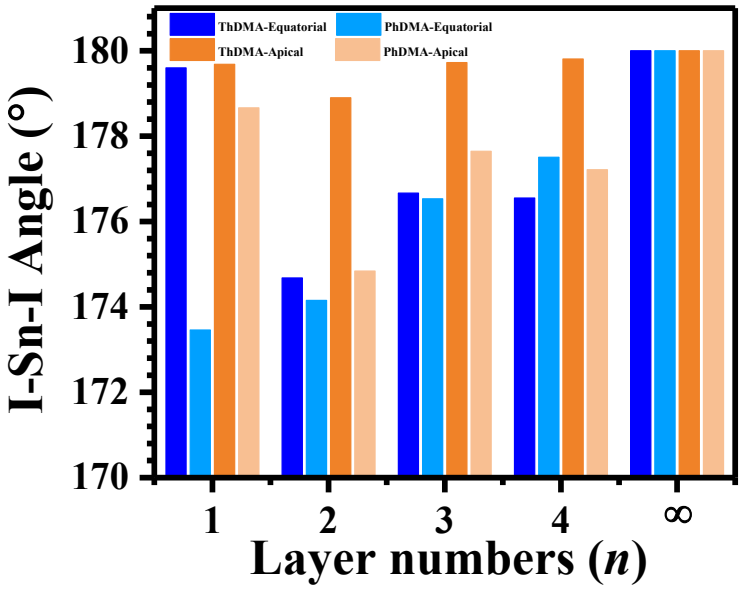

Figure S31. The calculated equatorial and apical I-Sn-I angles of (ThDMA)$Cs_{n-1}Sn_nI_{3n+1}$ and (PhDMA)$Cs_{n-1}Sn_nI_{3n+1}$ perovskites.

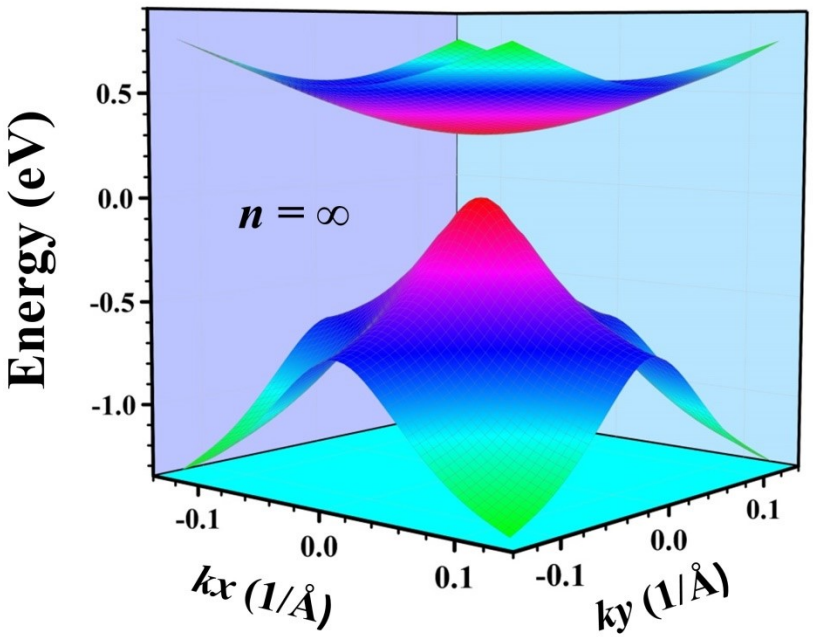

Figure S32 . Calculated 3D band structures of $CsSnI_3$ perovskites.

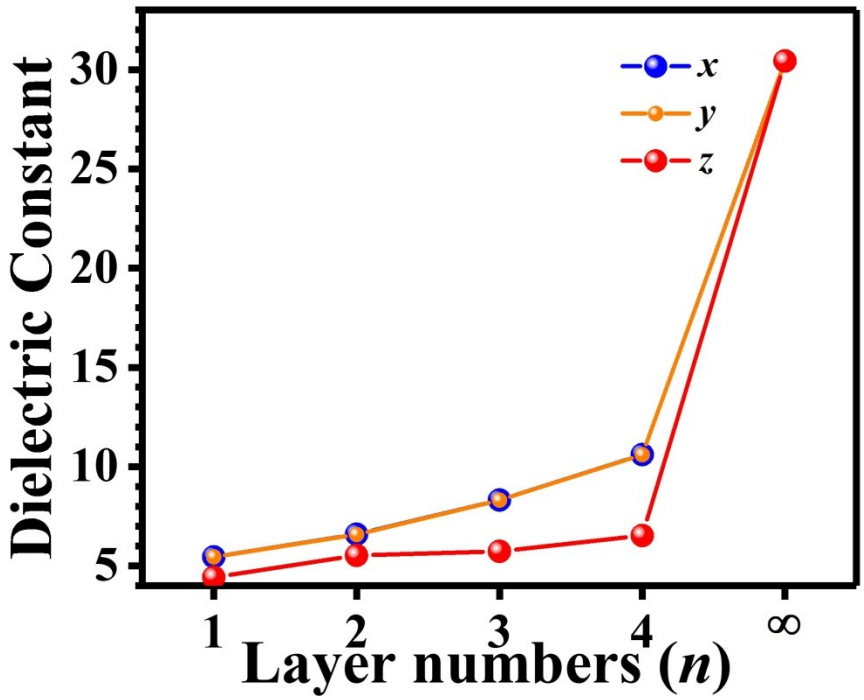

Figure S33. The dielectric constants of (ThDMA)$Cs_{n-1}Sn_nI_{3n+1}$ (n = 1-4 and ∞).

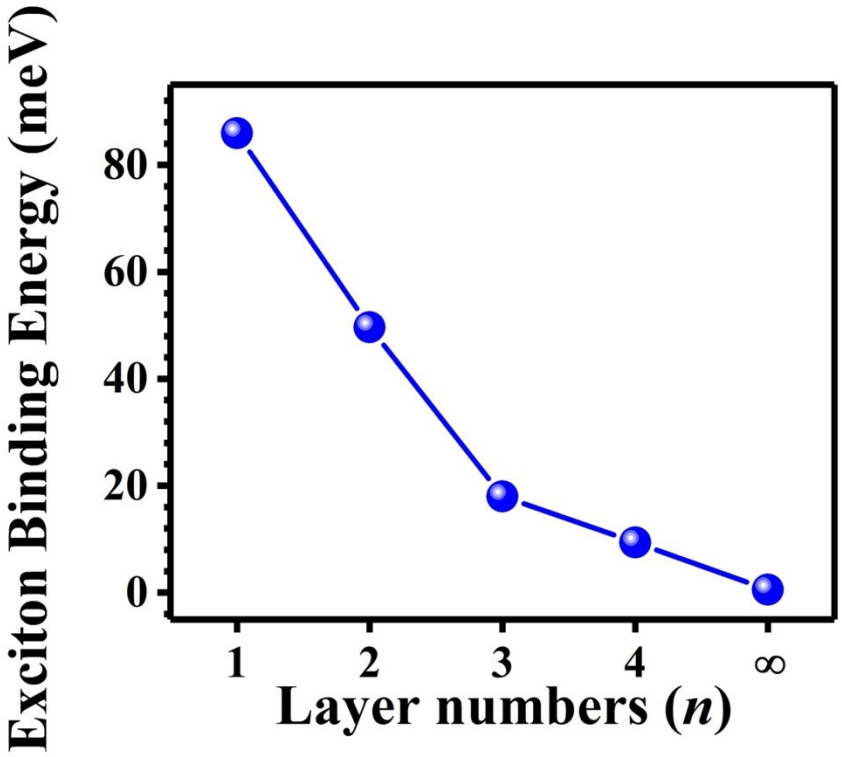

Figure S34. The exciton binding energies of (ThDMA)$Cs_{n-1}Sn_nI_{3n+1}$ (n = 1-4 and ∞).

Table S1. Calculated lattice parameters of (ThDMA)$Cs_{n-1}Sn_nI_{3n+1}$ (n = 1-4 and ∞) perovskites.

n	1	2	3	4	∞(unit cell)	References[1] (α-$CsSnI_3$)
a(Å)	12.040(5)	12.092(5)	12.316(3)	12.289(0)	6.210(7)	6.219(0)
b(Å)	12.041(3)	12.089(3)	12.316(4)	12.288(3)	6.210(7)	6.219(0)
c(Å)	12.813(6)	18.915(0)	25.380(3)	31.372(0)	6.210(7)	6.219(0)
α	90.005(8)	90.051(9)	89.997(2)	89.996(8)	90.000(0)	90.000(0)
β	89.994(1)	90.180(5)	90.000(5)	89.998(3)	90.000(0)	90.000(0)
γ	90.007(7)	90.106(6)	90.000(3)	90.003(3)	90.000(0)	90.000(0)
Number of atom	104	124	144	164	5	5

Table S2. Sn-I bond lengths, I-Sn-I angles and Sn-I-Sn angles of (ThDMA)$Cs_{n-1}Sn_nI_{3n+1}$ (n = 1) perovskites.

Label	i-th layer	1
Sn-I bond	Equatorial	3.1337(1)
	Apical	3.2028(4)
	Average	3.1682(7)
I-Sn-I angle	Equatorial	179.5986(9)
	Apical	179.6854(8)
	Average	179.6420(8)
Sn-I-Sn angle	Equatorial	147.8076(3)
	Apical	-
	Average	147.8076(3)

Table S3. Sn-I bond lengths, I-Sn-I angles and Sn-I-Sn angles of (ThDMA)$Cs_{n-1}Sn_nI_{3n+1}$ (n = 2) perovskites.

Label	i-th layer	1	2
Sn-I bond	Equatorial	3.1243(2)	3.1269(8)
	Apical	3.2132(6)	3.1912(5)
	Average	3.1687(9)	3.1591(2)
I-Sn-I angle	Equatorial	175.6956(3)	173.6599(3)
	Apical	178.9178(5)	178.8855(3)
	Average	177.3067(4)	176.2727(3)
Sn-I-Sn angle	Equatorial	150.8917(9)	150.7150(3)
	Apical	177.1394(8)	-
	Average	164.0156(3)	150.7150(3)

Table S4. Sn-I bond lengths, I-Sn-I angles and Sn-I-Sn angles of (ThDMA)$Cs_{n-1}Sn_nI_{3n+1}$ (n = 3) perovskites.

Label	i-th layer	1	2	3
Sn-I bond	Equatorial	3.1765(6)	3.07925(5)	3.1791(5)
	Apical	3.1963(9)	3.1840(8)	3.2064(5)
	Average	3.1864(7)	3.1316(7)	3.1928(0)
I-Sn-I angle	Equatorial	175.1237(3)	179.7021(5)	175.1773(0)
	Apical	179.7356(8)	179.9255(3)	179.5086(8)
	Average	177.4297(0)	179.8138(4)	177.3429(9)
Sn-I-Sn angle	Equatorial	151.6682(0)	178.8908(8)	153.9131(5)
	Apical	179.6293(3)	179.4192(0)	-
	Average	165.6487(6)	179.1550(4)	153.9131(5)

Table S5. Sn-I bond lengths, I-Sn-I angles and Sn-I-Sn angles of (ThDMA)$Cs_{n-1}Sn_nI_{3n+1}$ (n = 4) perovskites.

Label	i-th layer	1	2	3	4
Sn-I bond	Equatorial	3.1723(7)	3.0729(6)	3.0724(7)	3.1634(1)
	Apical	3.1879(4)	3.1595(6)	3.1451(5)	3.1697(3)
	Average	3.1801(6)	3.1162(6)	3.1088(1)	3.1665(7)
I-Sn-I angle	Equatorial	174.7466(8)	177.7831(5)	178.6861(6)	174.9933(3)
	Apical	179.8104(3)	179.8460(3)	179.7896(5)	179.7861(3)
	Average	177.2785(5)	178.8145(9)	179.2379(1)	177.3897(3)
Sn-I-Sn angle	Equatorial	151.2731(5)	177.8214(1)	178.6821(0)	152.5421(1)
	Apical	179.8007(5)	179.6580(5)	179.6094(8)	-
	Average	165.5369(5)	178.7397(3)	179.1457(9)	152.5421(1)

References

[1] L.Y. Huang and W. R. L. Lambrecht, *Phys. Rev. B*, 2013, **88**, 165203.